Measurement 189 (2022) 110508

Contents lists available at ScienceDirect

Measurement

journal homepage: www.elsevier.com/locate/measurement

Quantification of phase-based magnified motion using image enhancement and optical flow techniques

Nicholas A. Valente [a], Celso T. do Cabo [b], Zhu Mao [a,b,*], Christopher Niezrecki [a]

[a] Department of Mechanical Engineering, University of Massachusetts Lowell, Lowell, MA 01854, USA
[b] Department of Mechanical and Materials Engineering, Worcester Polytechnic Institute, Worcester, MA 01609, USA

ARTICLE INFO

Keywords:
Phase-based motion magnification
Image processing
Optical flow
Computer vision
Noncontact sensing
Motion extraction

ABSTRACT

Phase-based motion magnification (PMM) has been widely implemented in the field of vibration and structural health monitoring for its non-invasive nature to reveal hidden system dynamics. The approach has shown success in magnifying subtle structural oscillatory motions for system identification and observation of operating shapes. Although this method has been implemented and is becoming increasingly popular, the amount of physical motion associated with the degree of magnification has yet to be quantified. Within this work, a synthetic simulation containing an oscillating geometry is presented to quantify its magnified pixel displacement. Computer vision techniques including centroid detection and edge-feature tracking via optical flow are adopted to quantify the relation between amplification and true motion. The quantification techniques are also tested and verified on an experimental structure with the use of a high-speed optical sensing system. Motion artifacts distort the integrity of the magnified motion, which can pose problems for accurate quantification. Image enhancement techniques such as the two-dimensional Wiener filter and Total Variation Denoising (TVD) are used to smooth the high-frequency content that is observed following magnification. Associative error concerning a discrete shift of the Gabor wavelet is analytically derived to show the justification of spatial aliasing. An adjusted bound on magnification is presented to display the limitations of the technique, while providing insight into associated error. The results of this work will help to enhance PMM from a qualitative evaluation tool to a quantitative measurement tool of magnified displacements.

1. Introduction

The study of subtle motion has been an area of interest in the vibration community over the past decade. Sensors such as accelerometers and strain gauges have been used to capture dynamic characteristics from large structures. Due to the laborious setup using contact instrumentation, the use of cameras has proven to be a well adopted non-invasive technique for motion data acquisition. In the field of dynamics, structures tend to oscillate with subtle amplitudes, which may not appear to the naked eye. Although studies have shown, that PMM can be used for structural dynamics extraction qualitatively, there has yet to be an investigation into the quantitative capabilities and associated error of extracting magnified motion.

Liu et al. introduced a linear motion magnification approach, where imperceptible motion could be amplified and studied [1]. Most notably, Wadhwa et al. improved upon the linear magnification technique by manipulating the phase of an image where noise was translated rather than amplified with motion [2–3]. Since then, several modifications have been made to the algorithm for speed and noise improvements [4–7]. PMM has also been implemented in a wide variety of applications related to structural dynamics [8–13]. In particular, the use of PMM permitted computation of full-field operating deflection shapes in addition to fundamental frequencies of a structure that was subtly oscillating. [14–20]. Computation of modal parameters using a non-invasive approach was shown to be robust and require less contact and manual instrumentation [21–24]. Poozesh et al. demonstrated this approach for large-scale structures such as wind turbine blades [25].

In this work, image-processing techniques such as the two-dimensional Wiener filter and Total Variation Denoising (TVD) are implemented to smooth out the phase-based motion magnification artifacts that appears in distorted video. Quantifying magnified motion is achieved with the use of centroid and edge-feature tracking approaches as displayed in Fig. 1.

* Corresponding author at: Department of Mechanical and Materials Engineering, Worcester Polytechnic Institute, Worcester, MA 01609, USA.
E-mail address: zmao2@wpi.edu (Z. Mao).

https://doi.org/10.1016/j.measurement.2021.110508
Received 31 July 2021; Received in revised form 7 November 2021; Accepted 22 November 2021
Available online 24 November 2021

Nomenclature

Symbol	Name
α	Magnification factor
γ	Translation coordinates
$\delta(t)$	Image profile translation
δ'	Magnitude of original displacement
ϵ	Restriction factor
η	Neighborhood of pixels
λ	Regularization parameter
λ'	Spatial wavelength
μ	Local mean
ν	Average local variance
τ	Time shift
σ	Spatial smoothing parameter
σ'	Variance
ϕ	Peak-to-peak magnitude of magnified motion
$\phi(t)$	True displacement time history
$\widehat{\phi}(t)$	Approximate displacement time history
ω	Single frequency
ω_0	Selected frequency of filter
ψ	Scaling Factor

2. Literature background

Extraction of quantitative information in videos has been widely investigated over the past several decades. Developments in optical flow, tracking, and image filtering has served to enhance the capabilities of non-invasive measurement [26–29]. This in conjunction with PMM can serve as a means to extract the operating deflection characteristics as well as dynamic range of motion [30–33]. As a modification to [26], Tomasi introduced a feature window; such that, particular pixels are tracked from a reference characteristic frame [34]. The Kanade-Lucas-Tomasi (KLT) algorithm has been implemented in simple to complex computer vision problems ranging from face detection to image stabilization [35].

As magnification is increased, ringing artifacts (ghosting) appear due to the limited spatial support that is provided by the complex steerable pyramid [36]. Currently, there are a wide variety of smoothing algorithms that are available to aid in de-noising images. The two-dimensional Wiener filter serves as an adaptive noise removal approach; such that, noise variance is estimated in an image based on the average values of local variance [37]. For example, Rudin et al. introduced the total variation based approach, i.e. TVD, to tackle the noise removal process. This method poses an optimization problem that will return a denoised image based on a regularization parameter [38]. The elimination of ghosting artifacts will ultimately make quantifying magnified motion more simplistic and accurate. Adaptation of said algorithms for robust denoising of phase-based magnified videos has yet to be investigated in literature.

The novelty of the proposed work is the quantification of magnified motion and associative discrete error using different augmentation methods to enhance motion extraction. The implementation of the two-dimensional Wiener filter and TVD will suppress motion artifacts making quantification more simplistic and accurate. This could enable the use of PMM as both a qualitative and quantitative tool for non-invasive measurement. A comparison is made between the differing algorithms and their effect on the quantified displacement. The remainder of the paper is organized as follows: Section 3 presents the theoretical background while Section 4 introduces the test setup for experimental validation that is performed on a lab and synthetic data set. Section 5 provides an overview of the collected results and subsequent discussion. Finally, in Section 6 conclusions of the work are presented.

3. Theoretical background

3.1. Phase-based motion magnification (PMM)

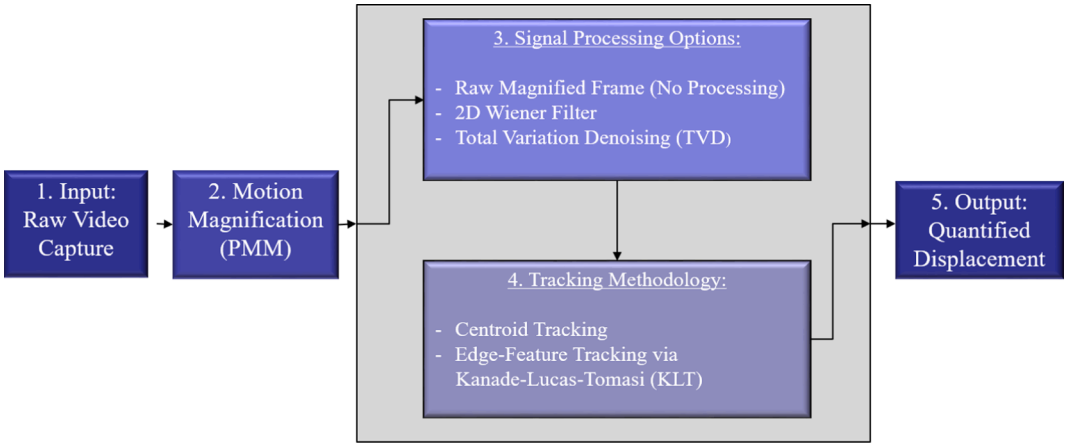

Fig. 1. Algorithm workflow diagram for the proposed work. Incremental steps include: (1) Video Acquisition, (2) PMM, (3) Signal Processing Options, (4) Tracking Methodology, and (5) Quantified Displacement.

There have been several improvements made to amplify subtle motion in video including alternative image pyramids and deep learning applied to motion magnification [2–4,31,39]. Displacement from phase information can be extracted and then magnified by decomposing the complex steerable pyramid based on the Fourier Shift Theorem; that is, the output displacement is proportional to the phase change between consecutive frames of the video in the frequency domain. As introduced by [2], PMM decomposes an intensity profile of an image, $f(x)$ where x represents pixels across the width of an image. This image profile is expressed as a sum of complex sinusoids in time, t, undergoing a global translation, $\delta(t)$ where

$$f(x+\delta(t)) = \sum_{\omega=-\infty}^{\infty} A_\omega e^{i\omega(x+\delta(t))}. \quad (1)$$

Similarly to the Fourier shift theorem, A_ω is representative of the respective amplitude while the phase $\omega(x+\delta(t))$ contains pertinent motion information. The separation of particular motion can be achieved by specifying bands of the filter that are represented by a single

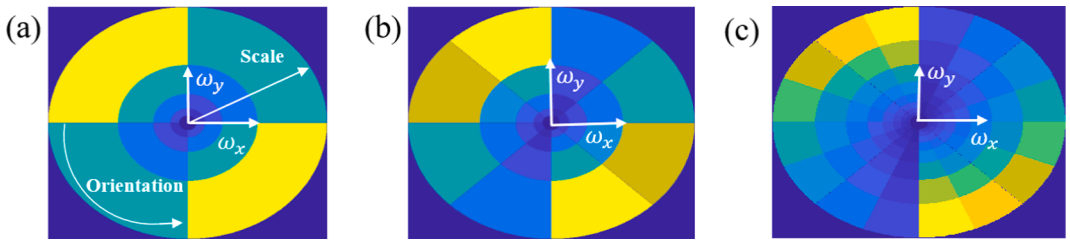

Fig. 2. Frequency Response of the Complex Steerable Pyramid [36]; (a) definition of orientation and scale, (b) Frequency Response of the Octave Filter Bank, (c) Frequency Response of the Half-Octave Filter Bank.

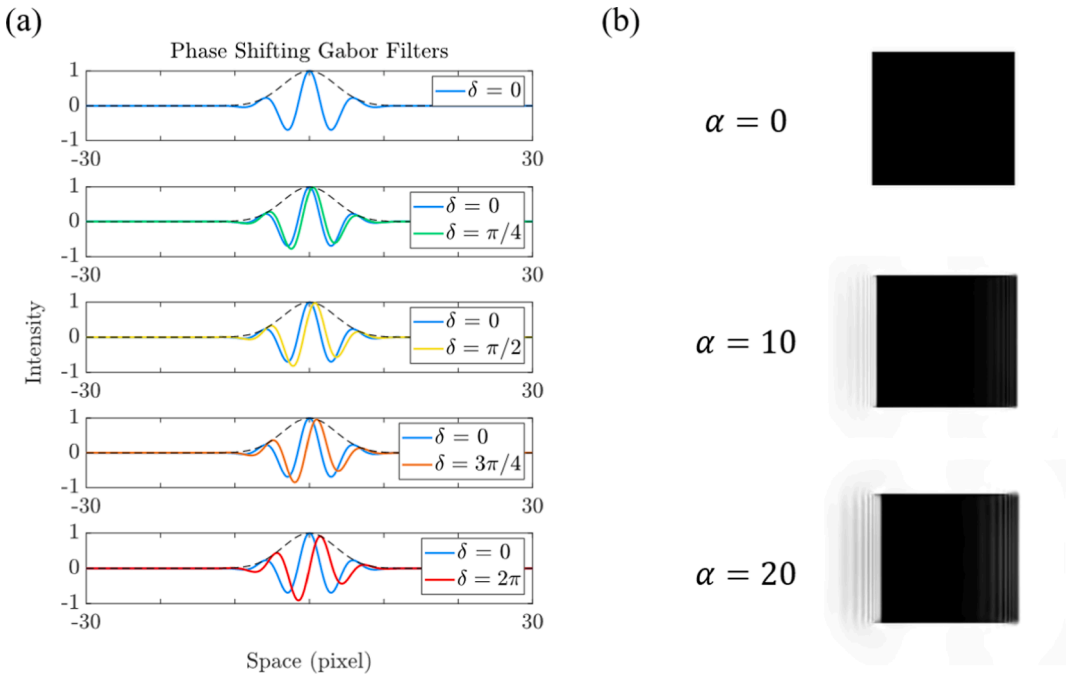

Fig. 3. (a) One-dimensional representation of phase shifting Gabor filters. As δ approaches $3\pi/4$, the Gaussian window or dotted curve truncates the signal which produces spatial aliasing resulting in ghosting artifacts, (b) Degradation of images due to the ghosting artifacts present in magnified video where true non-exaggerated motion is two pixels.

frequency ω . A band-passing of the phase in the temporal domain, removes the DC component of the phase shift such that

$$B_\omega(x,t) = \omega\delta(t). \tag{2}$$

Amplifying the motion in the sub-bands, $S_\omega(x,t)$ of the complex steerable pyramid comes as a result by multiplying the band-passed phase $B_\omega(x,t)$ by some magnification factor α . Reconstructing the intensity profile with magnified displacement yields

$$S_\omega(x,t) = A_\omega e^{i\omega(x+(1+\alpha)\delta(t))}. \tag{3}$$

It is then expressed that $S_\omega(x,t)$ is comprised of complex sinusoids that are modulated exactly $(1+\alpha)$ times. Collapsing the complex-steerable pyramid in each sub-band will result in a magnified image intensity profile $,f(x+(1+\alpha)\delta(t))$. The computation of local phase in each sub-band takes place at each scale and orientation of the filter as show in Fig. 2 (a). For visual representation, Fig. 2(b), and Fig. 2(c) display the frequency response of the octave and half-octave filter banks. The spacing between each orientation is correspondent to a base two frequency ratio. That is, for the octave and half-octave filter bank, the spacing between each orientation will be 2^1 and $2^{1/2}$ respectively for the angular direction. In the radial direction, the octave filter contains four scales while the half-octave contains eight. Having more orientations and scales in the frequency domain permit larger amplification of motion due to their support in the spatial domain.

Amplification of subtle displacement has been helpful in visualizing imperceptible motion; however, motion artifacts start to become a burden when dealing with large amplification factors. This occurs due to the complex steerable pyramid's limited spatial support once magnification exceeds the filters bound. An approximate one-dimensional representation of the complex steerable pyramid is a Dirac function that is shifted $\delta(t)$ by a Gabor filter [2]. These wavelets contain a Gaussian function with a specific width $,\sigma$ that attenuates the motion of the sinusoid underneath the bell curve. Eq(s). 4 through 7 are derived by Wadhwa et al. where the impulse response is defined as

$$S_\omega(x,t) = e^{-(x-\delta(t))^2/(2\sigma^2)} e^{2\pi i\omega_0(x-\delta(t))}. \tag{4}$$

A band-pass filtering and magnification of the phase at $t=0$ and t , yields

$$B_\omega(x,t) = 2\pi\omega_0\alpha\delta(t). \tag{5}$$

Therefore, the band-passed phase difference will shift the motion by $\alpha\delta(t)$ pixels. The bound-on magnification plays an important role in determining where exaggeration of true motion has reached a maximum. The appropriate bound on $\alpha\delta(t)$ is a constant, C [2]. As δ approaches $3\pi/4$, spatial aliasing begins to appear which leads to the ghosting artifacts that are generally seen in magnified video as show in Fig. 3. An L_1 normalized error for a particular phase shift is computed by comparing a true and Gabor shifted signal. The impulse response for a

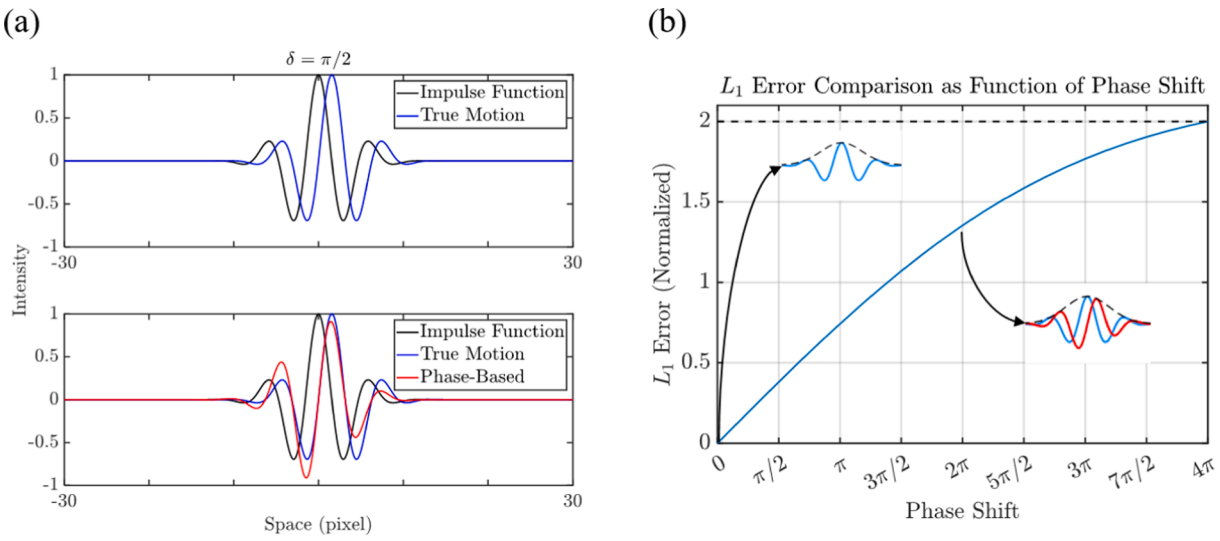

Fig. 4. (a) Phase shifted impulse function by $\delta = \pi/2$; the plot displays the difference in modulation using pure translation versus using Gabor wavelet, (b) L_1 error function for phase shifts δ .

Dirac function is defined in Eq. (4). The approximated shift , $S_\omega(x,t)$, that is attenuated by the Gaussian bell curve of Gabor wavelet is defined as

$$S_\omega(x,t) = e^{-x^2/(2\sigma^2)} e^{2\pi i \omega_0 (x-\delta(t))}. \tag{6}$$

Fig. 4 (a) depicts the difference in phase shift for the true and Gabor-shifted signal. For a discrete set of points, the L_1 error function in pixels is written from $j = (1,n)$ where n is the length of signal as

$L_1 = \sum_{j=1}^{n} \left| S_\omega(x(j),t) - S_\omega(x(j),t) \right|$, and

$$L_1 = \sum_{j=1}^{n} \left| e^{2\pi i \omega_0 (x(j)-\delta(t))} \left(e^{-\frac{(x(j)-\delta(t))^2}{2\sigma^2}} - e^{-\frac{x(j)^2}{2\sigma^2}} \right) \right|. \tag{7}$$

Fig. 4 (b) displays the L_1 norm error function from Eq. (7) comparing the true versus Gabor shifted signal. It should be noted that the suggested shift of $\pi/2$ represents one-quarter of a full cycle/wavelength. As aforementioned and depicted in Fig. 3 (b), the phase unwrapping that takes place past 2π will extend the provided spatial support; thus, the justification of ghosting artifacts. The generation of motion artifacts will make quantification of motion via computer vision more difficult due to their gray scale variation at the boundary. The implementation of two-dimensional filters will aid in suppressing said artifacts making quantification more accurate.

3.2. Two-dimensional wiener filter

Image filtering has been used in applications of PMM due to its ability to account for distortions that appear in video [40]. The two-dimensional Wiener filter is a computationally effective tool to smooth the ghosting artifacts that appear at large magnification factors. As introduced by [37], the two-dimensional Wiener filter first computes the local mean , μ, and variance , $\sigma^{'2}$, of an N -by- M image, X where

$$\mu = \frac{1}{NM} \sum_{n_1,n_2 \in \eta} X(n_1,n_2), \text{and} \tag{8}$$

$$\sigma^{'2} = \frac{1}{NM} \sum_{n_1,n_2 \in \eta} X^2(n_1,n_2) - \mu^2. \tag{9}$$

The specific coordinates , (n_1,n_2) are defined within the specified neighborhood of pixels η . As η increases, the computation time of the two-dimensional filter becomes larger due to the densely populated number of pixels. Following computation of Eq. (8) and Eq. (9), a denoised image , $\widehat{X}$, is computed using , ν^2, the average of the local variances defined in the pixel neighborhood η .

$$\widehat{X}(n_1,n_2) = \mu + \frac{\sigma^{'2} - \nu^2}{\sigma^{'2}} (X(n_1,n_2) - \mu) \tag{10}$$

The denoised image $\widehat{X}$ ideally would aid in smoothing the ghosting artifacts or ripples that appear following a desired magnification of subtle motion.

3.3. Total-variation denoising (TVD)

Posing an optimization approach to image enhancement can be an alternative to utilizing traditional image processing techniques. TVD, as introduced by [38] has shown to be useful in a wide variety of image processing problems including smoothing of medical imaging and signal enhancement [20,41]. An iterative process is used to compute the total variation between a noisy image f and a smoothed image u where ∇ is the differential operator. This processed is defined as

$$\frac{\partial u}{\partial t} = \nabla \cdot \left(\frac{\nabla u}{\|\nabla u\|} \right) + \lambda(f - u). \tag{11}$$

The regularization parameter λ ranges from 0 to 1 where the smoothing becomes more severe as it approaches its minimum value. It should be noted that when u is denoised, the total variation is equal to the gradient magnitude. This equivalency can only be achieved after many iterations and computation of the L_2 norm, which can become computationally expensive especially with larger images. Comparably to the two-dimensional Wiener filter, the denoised image u will display fewer ghosting artifacts than the original magnified frame f . Due to the smoothing of defined boundaries, edge-preservation may not be as robust compared to traditional image processing algorithms.

3.4. Centroid tracking

Computer vision approaches have been implemented over several decades to track pixelated motion [27]. The centroid tracking of a particular region of interest first begins with applying a threshold to compute a binary image. Global thresholding is applied to individual frames; such that, pixel intensities are converted to 0 or 1 for each coordinate (i,j) . These intensities are based on an adaptive grayscale threshold , h, that is found in the image , I . A binary image B is defined as

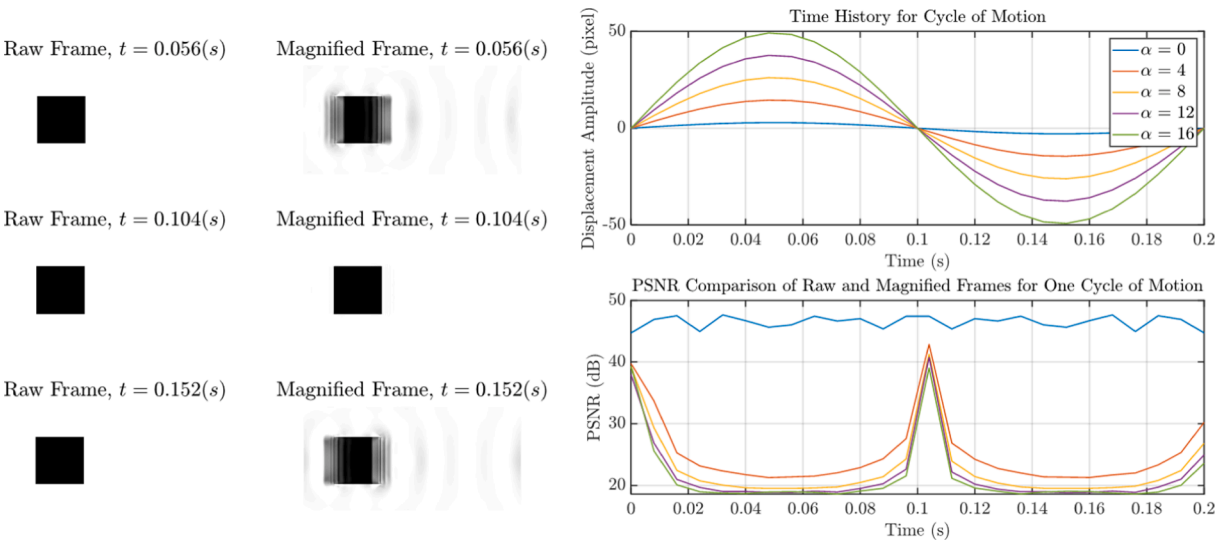

Fig. 5. A qualitative assessment of frame distortion due to an increase in magnification factor, where $\alpha = 10$.

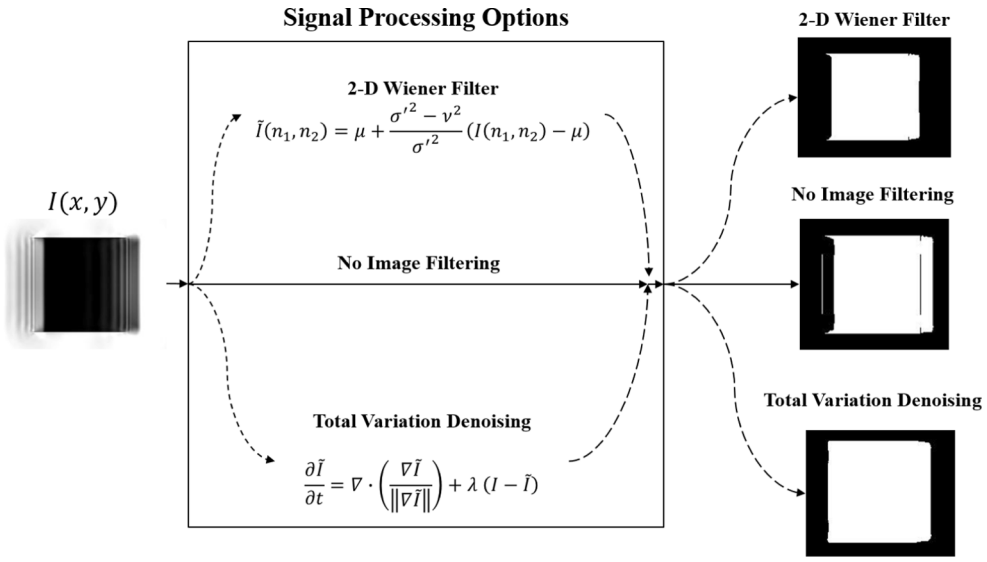

Fig. 6. Binary frame comparison of various methods where I is the magnified image and $\mathcal{I}$ is the processed frame. For the no image filtering case , $\mathcal{I} = I$.

$$B(i,j) = I(i,j) > h. \tag{12}$$

From this point, it becomes simplistic to compute the coordinates for the region of interest. The x and y coordinates for the n -by- m frame are expressed as

$$\overline{x} = \frac{\sum_{i=0}^{n-1}\sum_{j=0}^{m-1} jB(i,j)}{A}, \overline{y} = \frac{-\sum_{i=0}^{n-1}\sum_{j=0}^{m-1} iB(i,j)}{A}. \tag{13}$$

In this context, A is regarded as the area of a binary image B . There are differing approaches from the traditional centroid tracking, which aim to pinpoint boundaries surrounding the region of interest.

3.5. Edge tracking via Kanade-Lucas-Tomasi feature tracker (KLT)

Optical flow algorithms have been widely implemented to quantify changes in pixel intensity for motion extraction [26]. The use of optical flow helps estimate motion in images by evaluating a pixel's intensity over time. Tomasi et al. made improvements to the traditional Lucas-Kanade (LK) optical flow algorithm to track select regions of interest within an image [34]. This ultimately produced the enhanced Kanade-Lucas-Tomasi (KLT) algorithm. When evaluating subtle motion in video, edge-features are presented as an alternative to traditional centroid tracking approaches [35]. The KLT algorithm pays heavy attention to the squared sum of the gray difference between frames. This difference is only tracked in a window or region of interest that is specified by the user. The position of sequential images $I(x, y, t)$ and $I(x, y, t+\tau)$ at time t and $t+\tau$ satisfy

$$I(x, y, t+\tau) = I(x - \Delta x, y - \Delta y, t), \text{where} \tag{14}$$

The corresponding displacements here are defined as Δx and Δy . Specifying a region of interest at a reference frame, $J(x, y, t)$ and a sequential frame $K(x, y, t+\tau)$ yields

$$J(X - \gamma) = J(x - \Delta x, y - \Delta y, t), \tag{15}$$

$$K(X) = K(x, y, t+\tau). \tag{16}$$

X is comprised of the image coordinates (x, y) for respective frames where our shifted displacements is γ . Second order moments of the image can now be obtained by computing the gradient of the image g in the (x, y) directions

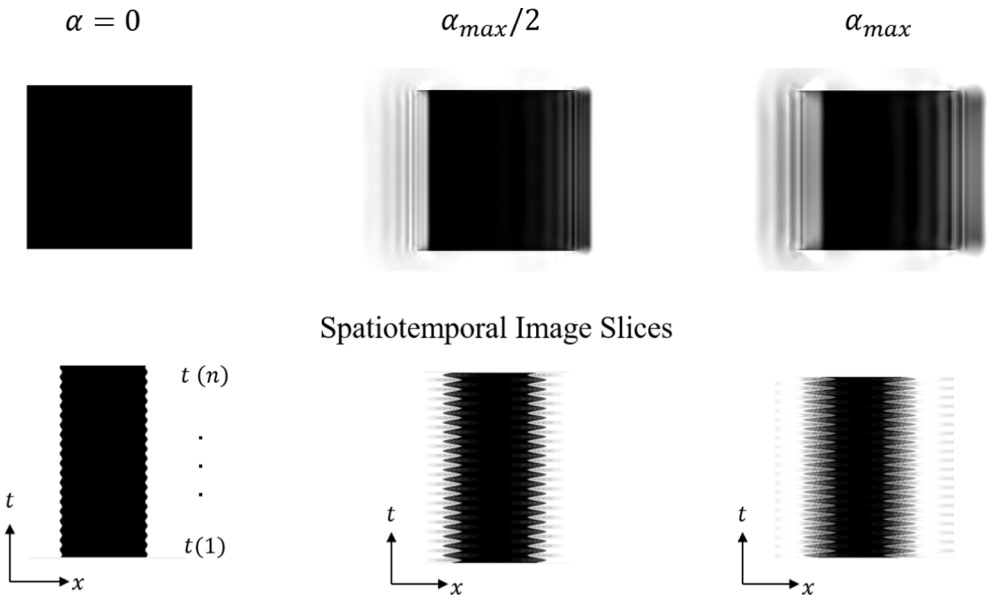

Fig. 7. Spatiotemporal slices of images for varying degrees of magnification. α_{max} is computed using a 400 × 400 (pixel) frame to determine λ.

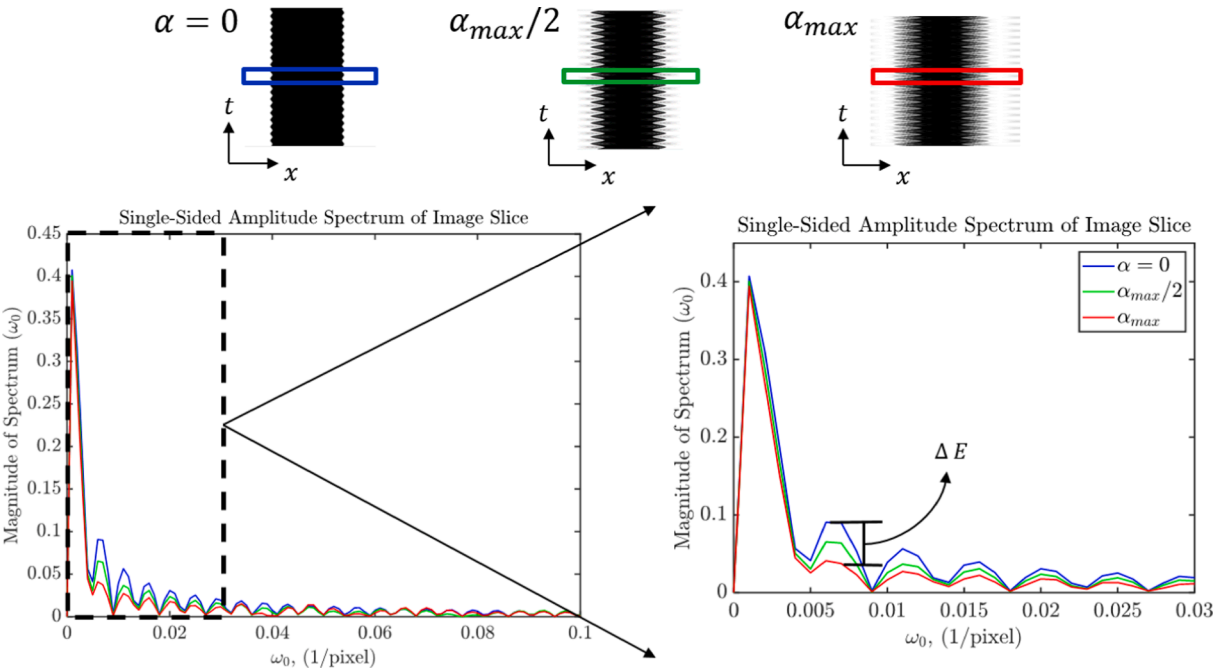

Fig. 8. FFT of spatiotemporal image slice where α ranges from 0 to α_{max} . As α increases, the difference in power spectrum amplitude ΔE is depreciated in the side lobes.

$$Z = \iint g(X)g^T(X)dX = \iint \begin{bmatrix} g_x^2 & g_x g_y \\ g_x g_y & g_y^2 \end{bmatrix} dxdy \tag{17}$$

This sets up the final solution to obtain the approximate translation γ where

$$\gamma = Z^{-1} \iint [J(X) - K(X)]g(X)dxdy. \tag{18}$$

For small regions of interest with a distinct boundary, the use of the KLT algorithm will be useful in tracking subtle displacement due to its pixel-by-pixel operations. In the following sections, quantified displacements draw comparisons between centroid versus the edge-feature tracking for a sequence of images or magnified video.

4. Test setup for experimental validation

4.1. Implementation of 2D filtering

There are several differing parameters available to the user when using PMM, which without familiarity can affect magnified results. Currently, magnification factor, α is arbitrarily selected based on the visual representation of motion. This work aims to compute an appropriate magnification factor for quantification of exaggerated motion. The test case will be a black square that is given a particular size and amplitude of motion. Fig. 5 displays a rigid geometry undergoing magnified translation for one-full cycle. Once the region of interest reaches it maximum or minimum, there is a significant drop in peak-

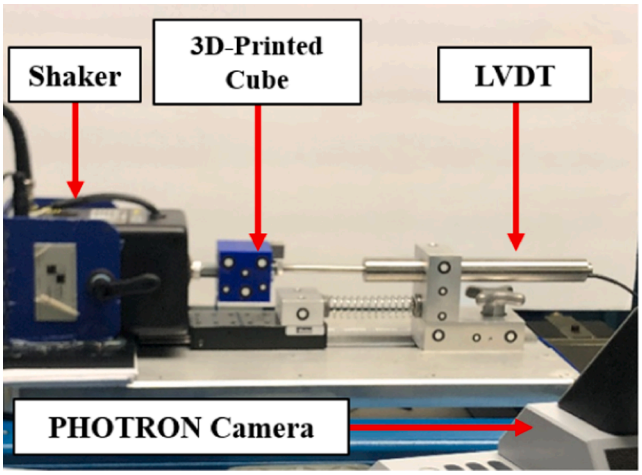

Fig. 9. Experimental test structure using PCB Smartshaker™, 3-D Printed Cube (region of interest), and LVDT.

signal to noise ratio (PSNR) when comparing the purely translated versus magnified frames. On the contrary, once the region reaches its equilibrium position, the PSNR is restored due to the limited distortion when comparing the raw versus magnified frames. Even at low values of α , frame distortion is still present which provides necessity in implementing image filtering such as the two-dimensional Wiener filter and TVD.

Fig. 6 displays binary images following magnified translation for filtered and non-filtered frames. As a result of Eq. (12), each pixel in the frame will be converted to a 0 or 1 intensity value. Due to the grayscale variation of the ghosting artifacts, the amplified displacement may not be well represented in a binary image due to the adaptive thresholding. Shown in Fig. 6, the use of Eq. (10) and Eq. (11), smooth the boundary, such that adaptive thresholding will not affect the magnified result. Ultimately, this places limitations on using a centroid-based quantification approach due to applying an improper image threshold prior to computing Eq. (13).

4.2. Determination of magnification factor for accurate quantification

As presented in the previous section, a selection of α drastically affects the results of magnified data. Wadhwa et al. define the bound on magnification for the half-octave filter bank as

$$\alpha < \frac{\lambda^{'}}{2\delta^{'}} \tag{19}$$

where $\lambda^{'}$ is defined as the spatial wavelength and $\delta^{'}$ is the magnitude of the original displacement [2]. The necessity to stay within the bounds of magnification plays a key-role in determining an accurate quantitative assessment of exaggerated motion. To compute the limit of α, a simple case of a rectangular region of interest will be examined. Spatial frequency , ω_0, is computed using the width of the image in pixels. The reciprocal of ω_0 is equivalent to λ' . The increase in λ' supports larger α due to the gain of spatial support. Although the maximum α is computed, quantification will be more difficult as magnification approaches its theoretical maximum. Eq. (20) presents a modification of the derived bound by Wadhwa et al. [2] to ensure accurate quantification of motion, where ϵ is a constant restriction factor.

$$\alpha_{max} < \frac{\lambda^{'}\epsilon}{2\delta^{'}} \tag{20}$$

As ϵ decreases, the maximum α is subsequently decreased resulting in less ghosting artifacts, which simplifies motion extraction. This can visually be proven in the frequency domain. For example, Fig. 7 displays the spatiotemporal slices of a frame from $t(1)$ to $t(n)$ where n is a distinct instance of time. It can be seen that as α is increased the region of interest's edges become less smooth and more jagged. The jagged edges are representative of the degradation that takes place due to ghosting artifacts.

The motion artifacts become more evident at the boundary once

Table 1
Synthetic video parameter selection prior to quantification.

Synthetic Video Independent Variable Selection	
$\delta^{'}$, Peak-to-Peak Displacement Amplitude of Motion (pixel)	5.8
Frequency of Motion (Hz)	5
Sampling Frequency (Hz)	125
Frame Dimension (pixel)	500 × 1000
Box Dimension (pixel)	220 × 220
Filter Bank	Half-Octave
α, Magnification Factor	0–12
σ, Spatial Smoothing Parameter (pixel)	0
Image Filtering Properties	
2-D Wiener Filter, η (pixels)	(15,15)
Total Variation Denoising, λ	0.2

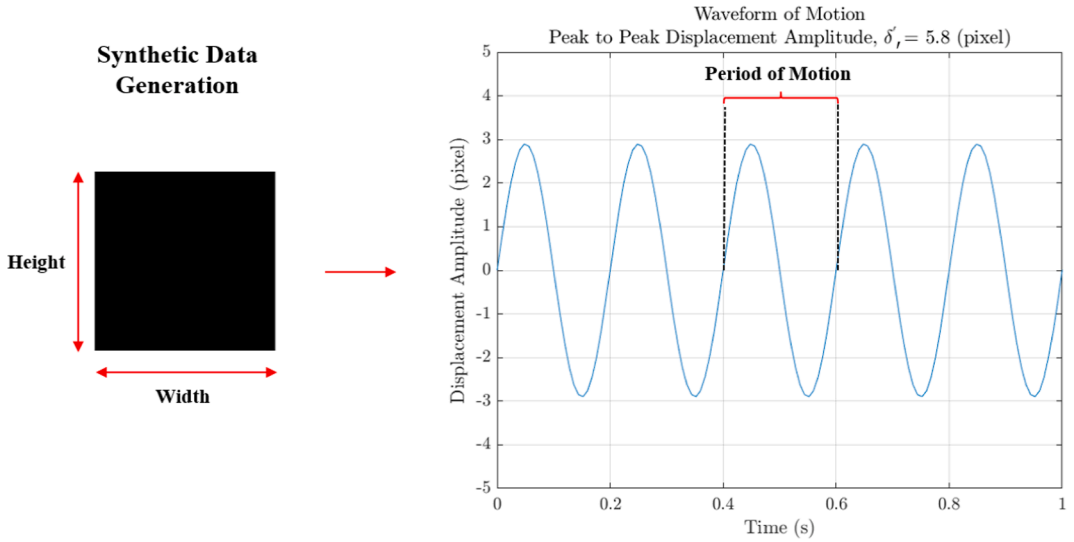

Fig. 10. A synthetic region of interest that is given horizontal sinusoidal motion with a specific frequency and displacement amplitude.

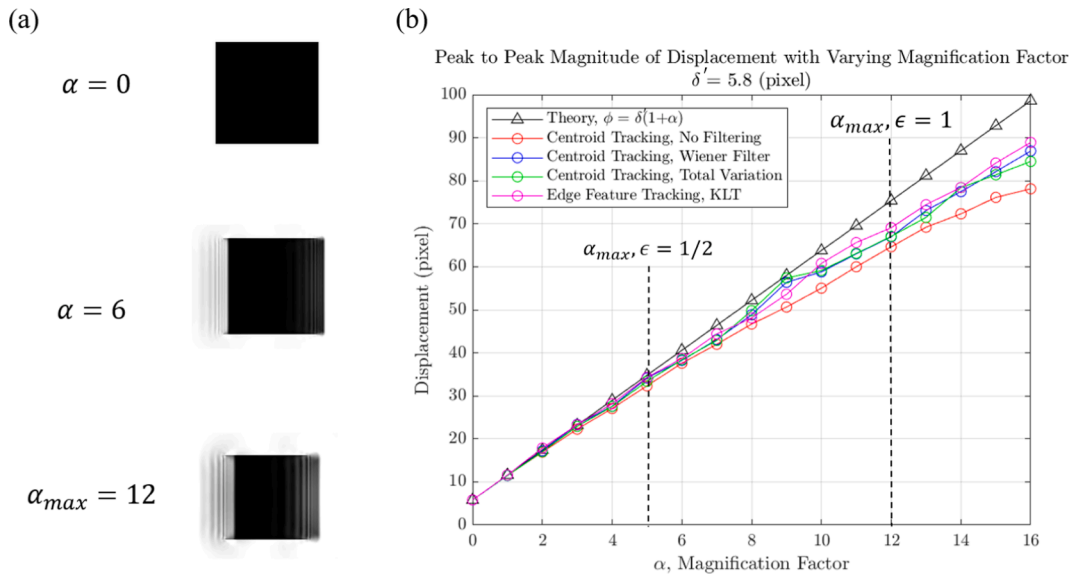

Fig. 11. Quantification of magnified displacement for synthetic data; (a) magnified images at $\alpha = 0, \alpha_{max}/2$, and α_{max} , (b) Comparison of peak-to-peak displacement amplitude for varying α .

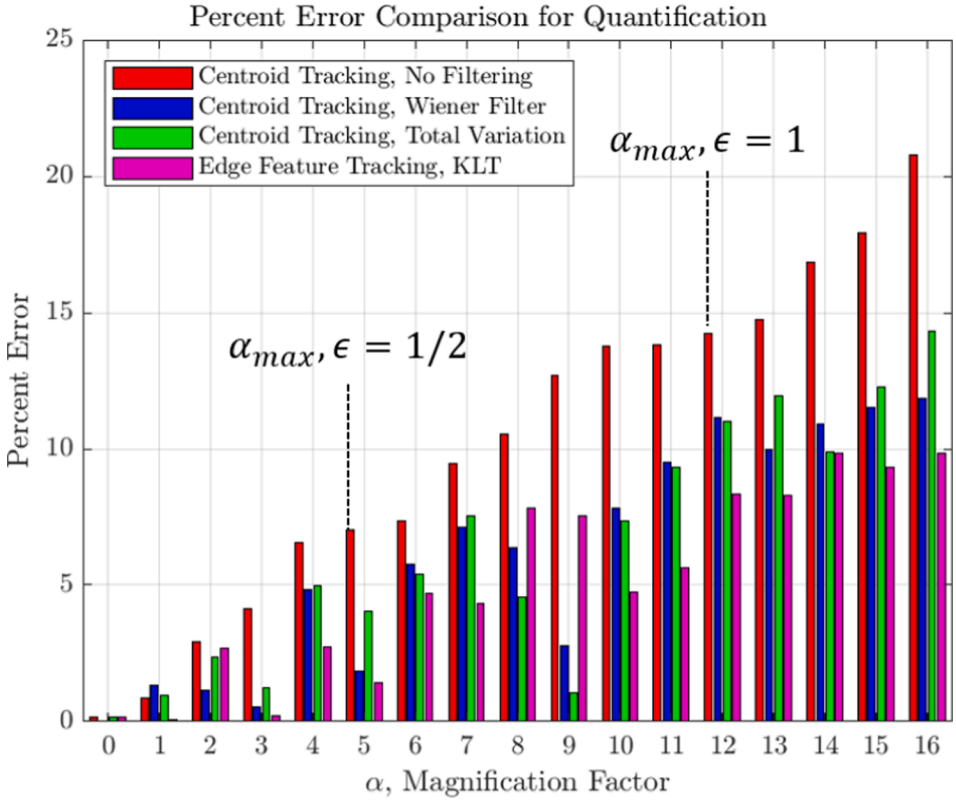

Fig. 12. Quantification of error comparison for computed peak-to-peak magnitudes of displacement.

Table 2
Synthetic data scaling factors (ψ) used to correct limitations of quantification measurements when compared to the theoretical trend line.

Tracking Methodology	Scaling Factor (ψ)	R^2
Centroid Tracking, No Filtering	1.221	0.9956
Centroid Tracking, Wiener Filter	1.126	0.9976
Centroid Tracking, Total Variation	1.152	0.9951
Edge-Feature Tracking (KLT), No Filtering	1.104	0.9987

motion is amplified. As aforementioned, a two-dimensional rectangular region of interest can be evaluated as a rectangular pulse function for a one-dimensional case. These functions are well characterized in the frequency domain, where the Fourier transform of a rectangular function is a *sinc* function. The power spectrum at specific magnification factors can be evaluated by taking the Fast Fourier Transform (FFT) of a spatiotemporal slice. Fig. 8 depicts the evaluated image slices in the frequency domain. As α reaches a maximum, the high-frequency components of the signal are compromised due to magnification ghosting

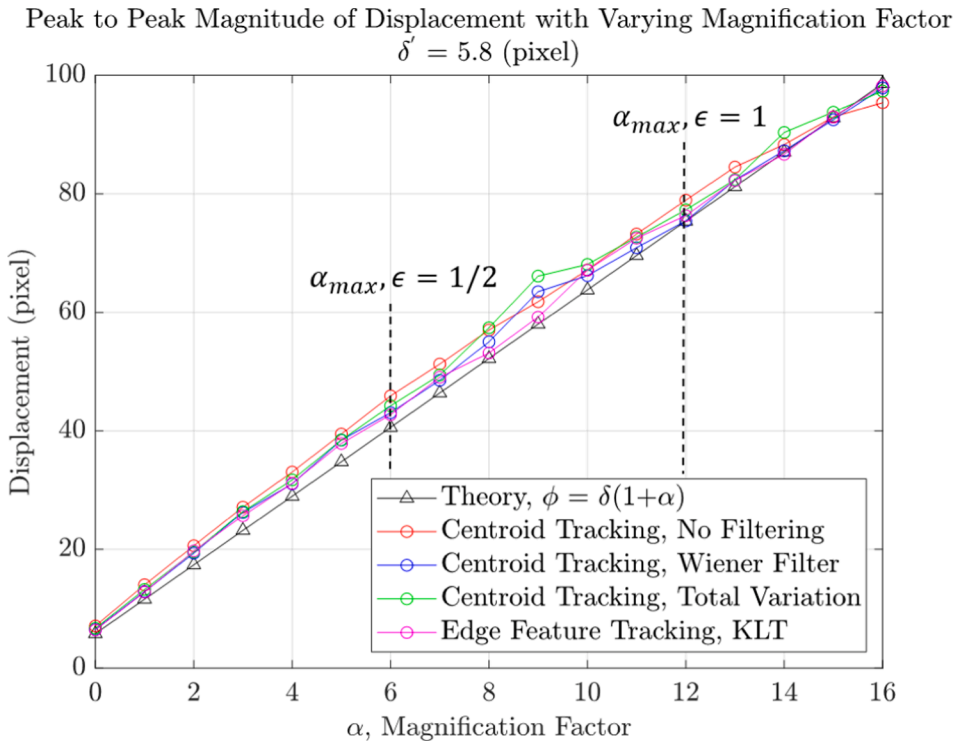

Fig. 13. Scaled magnitudes of displacement to match that of the theoretical curve, Eq. (21) for synthetic data.

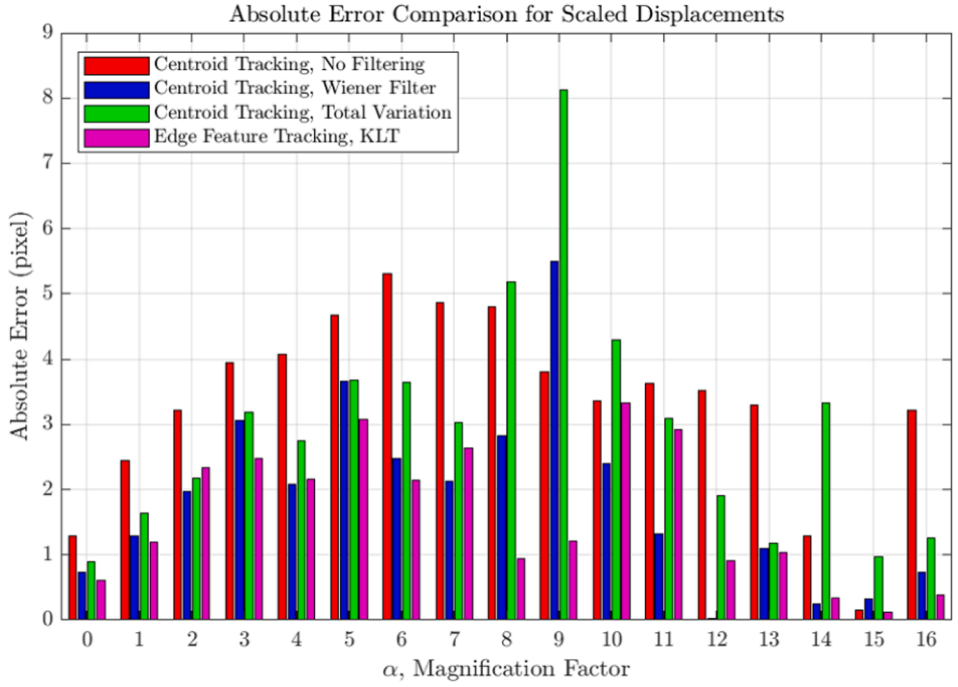

Fig. 14. Absolute error comparison of scaled displacements for synthetic data.

artifacts which limits it potential for motion extraction. It can be deduced that quantification error at α_{max} will be larger due to the larger difference in the power spectrum ΔE when comparing magnified and unmagnified image slices. By reducing the maximum α by half, the quantification boundary will be reduced. This is a direct result of conserving the signal's power post magnification.

4.3. Experimental verification setup

The objective of PMM is to amplify subtle motion in video for further structural dynamic analysis. The use of high-speed cameras has been integral in capturing subtle motion and pose as a suitable non-invasive approach to data analysis. Fig. 9 captures the experimental test structure that is used to quantify a baseline motion measurement using a Linear Variable Differentiable Transformer (LVDT). A PCB Miniature

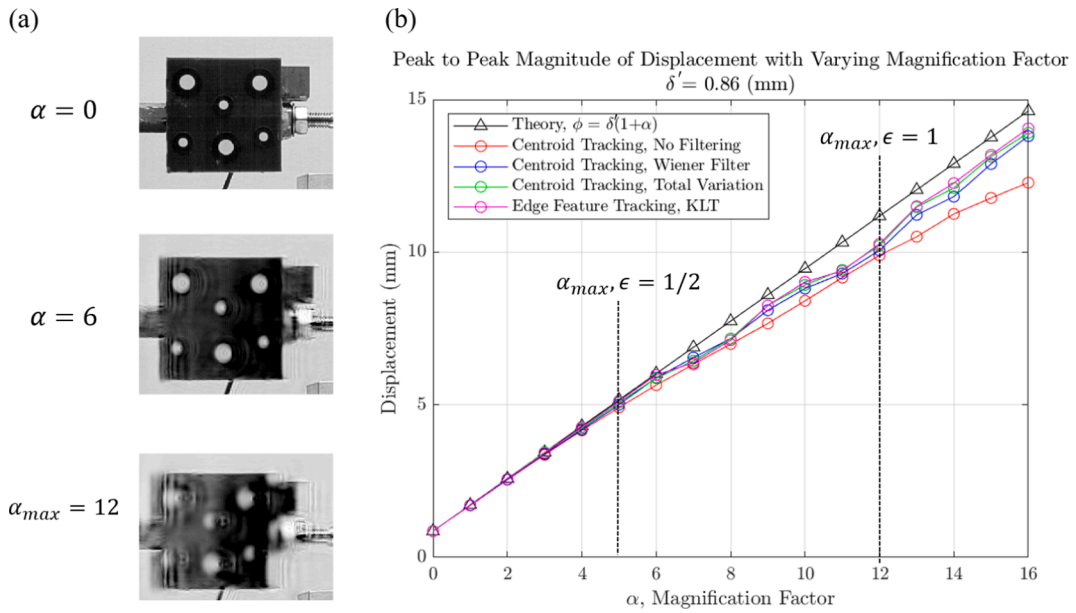

Fig. 15. Quantification of magnified displacement for experimental structure data; (a) magnified images at $\alpha = 0, \alpha_{max}/2$, and α_{max} , (b) Comparison of peak-to-peak displacement amplitude for varying α .

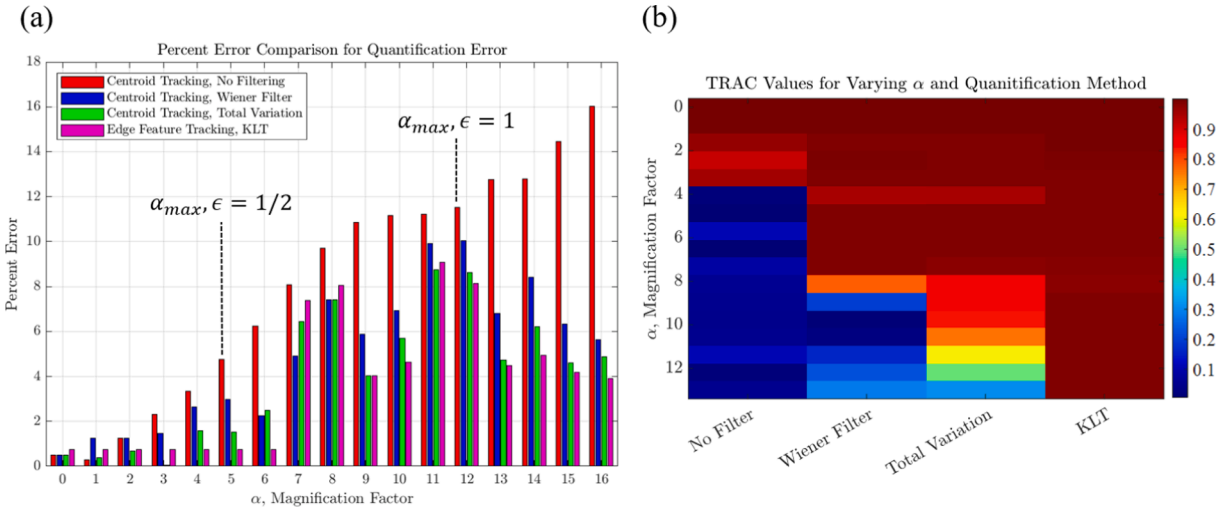

Fig. 16. (a) Quantification error comparison of computed peak-to-peak displacement magnitudes for experimental structure data, (b) TRAC values of experimental data time history for varying magnification factor and quantification technique.

Electrodynamic Shaker is used for excitation of the three-dimensional cube, while a single 4-megapixel PHOTRON high-speed camera captures data at 125 (fps). The working distance is 50 (cm) with a corresponding calibration factor of approximately 0.15 (mm/pixel).

A 5 (Hz) sine-wave pulse was applied to the 3D-printed cube to generate subtle motion. The peak-to-peak magnitude of the displacement time history is 0.86 (mm). According to [2], the magnified motion should be equivalent to $(1+\alpha)$ times true motion. This can concisely be expressed as,

$$\phi = \delta'(1+\alpha) \tag{21}$$

where ϕ is the peak-to-peak magnitude of magnified motion, α is magnification factor, and δ is the peak-to-peak magnitude of unmagnified motion. Once the data is collected, a α_{max} value is computed using Eq. (20).

4.4. Synthetic data generation

A synthetic video is generated in this work to mimic that of the experimental setup that would contain a moving object. As shown in Fig. 10, the video contains a rigid square geometry that will oscillate back and forth at a particular frequency and amplitude that is specified by the user. Following the initial generation of the video, a selection of PMM parameters such as: filter bank, magnification factor and spatial smoothing parameter are designated. Table 1 outlines the selected parameters for the synthetic video test including the image filtering considerations.

The parameters that were chosen closely resemble the experimental test; such that, comparisons could be drawn between synthetic and experimental structure data. For example, δ' was determined using the 0.86 (mm) displacement and corresponding calibration factor from the experimental validation test. It should be noted that the upper bound on α is determined using Eq. (20) where $\epsilon = 1$. Relaxing the restriction factor ϵ will permit evaluation of how well magnified motion can be

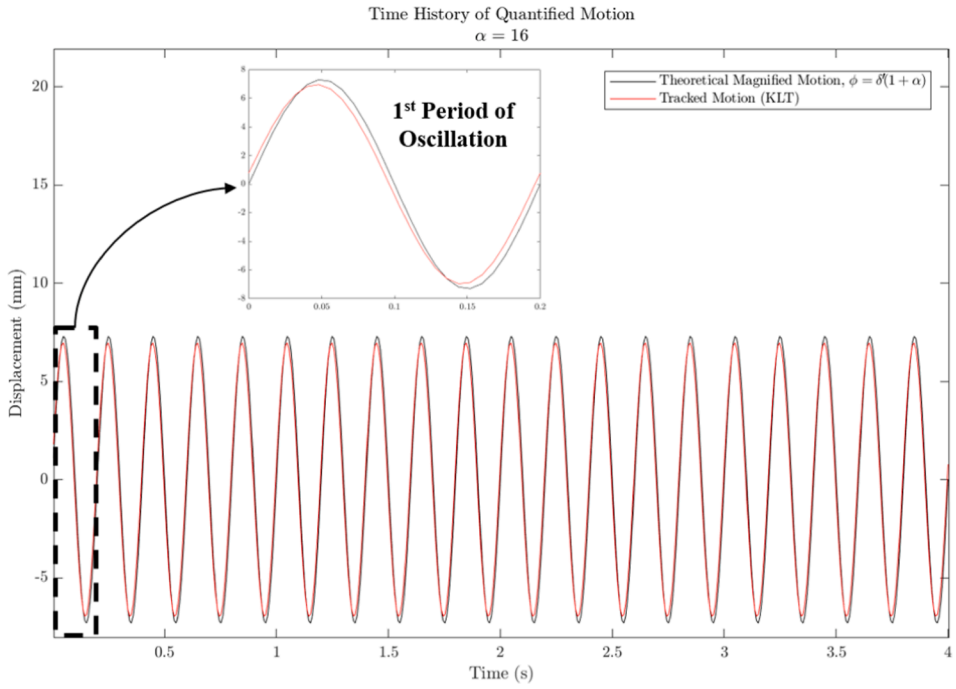

Fig. 17. Comparison of ideally magnified motion versus tracked motion via KLT. The TRAC value for comparing the two curves is 0.9871.

Table 3
Experimental data scaling factors (ψ) used to correct limitations of quantification measurements when compared to the theoretical trend line.

Tracking Methodology	Scaling Factor (ψ)	R^2
Centroid Tracking, No Filtering	1.170	0.9980
Centroid Tracking, Wiener Filter	1.060	0.9983
Centroid Tracking, Total Variation	1.052	0.9984
Edge-Feature Tracking (KLT), No Filtering	1.041	0.9987

quantified at α_{max} . The peak-to-peak displacement amplitude, $\delta^{'}$ was determined based on an experimental structure experiment test; such that, comparisons could be drawn between synthetic and experimental structure data. Following the determination of all parameters, quantification of motion is computed using both centroid detection and edge-feature tracking.

5. Results and discussion

5.1. Synthetic data test results

Quantification of exaggerated motion is achieved using unprocessed

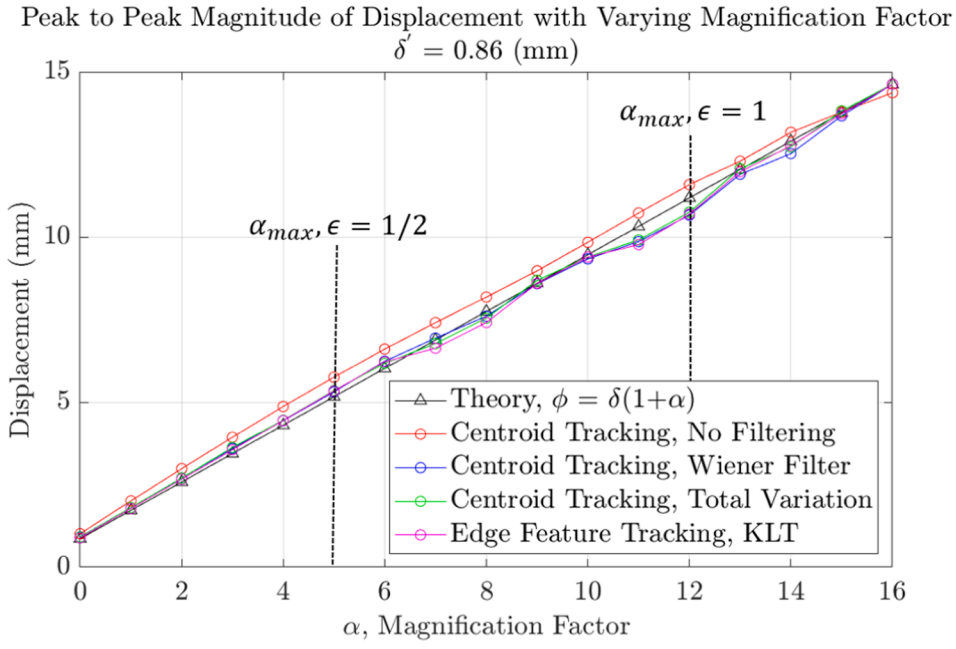

Fig. 18. Scaled magnitudes of displacement to match that of the theoretical curve, Eq. (21) for the experimental structure data.

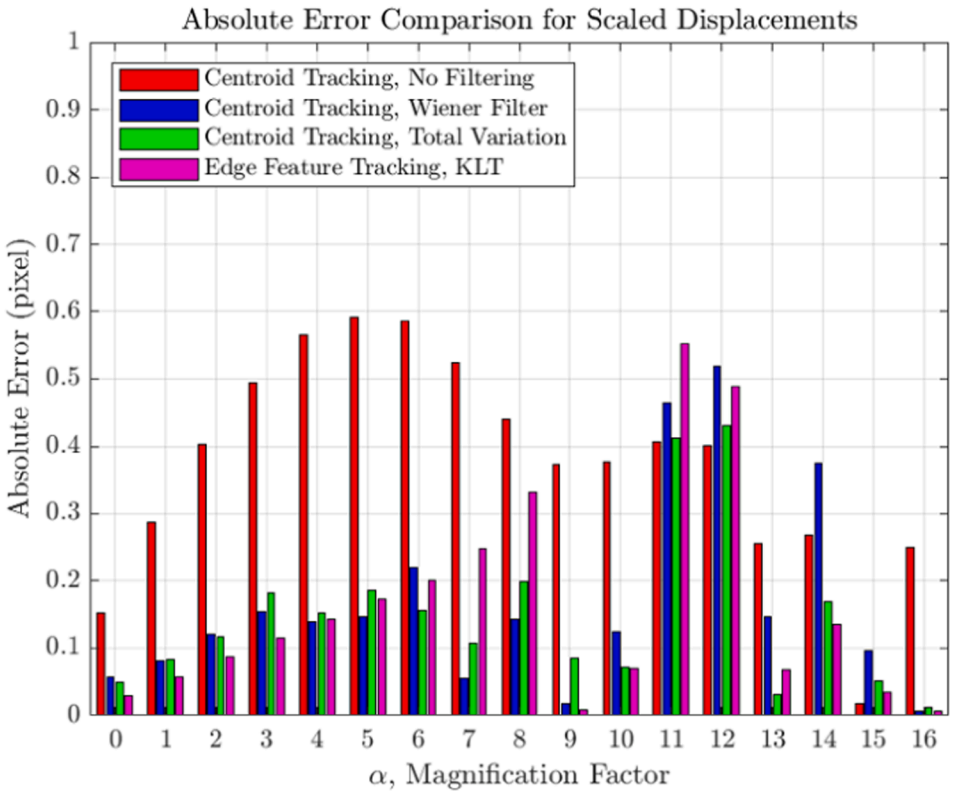

Fig. 19. Absolute error comparison of scaled displacements for experimental structure data.

or raw images and filtered magnified frames. For comparison purposes, the parameters selected for image filtering in Table 1 were used for both the experimental structure and synthetic test. Fig. 11 displays the quantified motion with α ranging from 0 to 16. Eq. (21) is used as comparative magnified motion that Wadhwa et al. suggests in the original work [2]. As shown in the figure, the image-enhancement methods greatly affect the centroid based tracking approach. This is attributed to smoothing the ghosting artifacts that appear once the image's phase is wrapped through 2π . The discrepancies in quantified amplitude at larger values of α are attributed to the assumptions made with both the centroid and edge feature tracking techniques. The restriction factor presented in Eq. (20) not only limits magnification, but also ensures accurate quantification. To account for inaccuracy in scaled data, absolute error quantifies the discrepancy between the theoretical target values (ϕ) versus the experiment results of peak-to-peak amplitude δ' multiplied by $(1 + \alpha)$. Eq. (22) computes the absolute error e with respect to the increase in magnification factor α .

$$e = \frac{|\phi - (\delta^{'}(1+\alpha))|}{\phi} \bullet 100\% \tag{22}$$

Fig. 12 displays the error associated with each quantification method.

The percent error comparison displays that the centroid tracking algorithm without image filtering does not perform as well as the proposed alternative methods. An empirical scaling factor, ψ is applied to the magnitudes of displacement using the difference in slope between each method and the theoretical curve. A first order assumption using a linear least square approach was used to compute corresponding scaling factors. This scaling factor is used to correct for the limitations of quantification assumptions due to the ghosting artifacts and could prove to be useful if displacement measurements are not known a-priori. Table 2 lists the scaling factors used for each approach, while Fig. 13 depicts the scaled magnitudes of displacement amplitude. Fig. 14 displays the quantified absolute error associated with each method and magnification factor.

5.2. Experimental data test results

Similarly, for the experimental structure experiment, Figs. 15 and 16 (a) display the magnitude of quantified motion and associative percent error using Eq. (22), respectively. Additionally, Fig. 15 (b) depicts the time-response assurance criterion (TRAC) values for each respective quantitative approach at differing magnification factors. A TRAC value is used to draw comparison between a theoretical and measured time-history. Here, the true motion $\phi(t)$ will be compared to the approximate displacement time curve $\widehat{\phi}(t)$ for each quantification method. The TRAC equation is expressed as,

$$TRAC = \frac{\left(\phi(t)^T \widehat{\phi}(t)\right)^2}{\left(\phi(t)^T \phi(t)\right)\left(\widehat{\phi}(t)^T \widehat{\phi}(t)\right)} \tag{23}$$

In Eq. (23), a value of unity represents perfect correlation where zero represents no correlation between the two discrete signals. Fig. 17 displays the overlayed time history of the ideal magnified displacement versus the tracked motion via KLT.

Similarly to the synthetic data experiment Table 3 lists the scaling factors used for each approach. In addition, Fig. 18 depicts the scaling factor for each individual quantification approach for the experimental structure experiment. Comparatively to the synthetic test results, Fig. 19 quantifies the absolute error for each method at individual magnification factors. Glancing at the results, the KLT algorithm proves to be the best approach among the methods investigated for tracking due to its ability to distinguish and interpolate between dark and light boundaries for magnified motion extraction. Due to the categorical nature of creating a binary frame, the centroid approach is more vulnerable to discarding a group of pixels that could prove to be important for quantification. Also the tracking performed on the experimental video was superior to that of the synthetic test due to the grayscale transition from light to dark. The synthetic data containing a cluster of dark pixels

on a bright background provided more artifacts due to the distinctive transition between edge features (high) and low frequency content in images.

6. Conclusion

In this work, phase-based motion magnification is used to extract quantitative measurement of magnified motion. Up until this point, PMM has solely been used to qualitatively show exaggerated motion, frequency of motion or deflection characteristics. Associative error is also derived for the Gabor-wavelet undergoing translation by an arbitrary phase shift. Two methods are introduced to quantify magnified motion: centroid tracking, edge-feature tracking via KLT. Also, additional image-enhancement filters are presented to serve as a tool for smoothing of ghosting artifacts that appear at larger magnification factors. Continuation of this work could center on automating determination of particular parameters such as regularization (λ) and thresholding (th) with respect to magnification factor. Analysis of quantified data for synthetic and experimental structure tests is presented, where a restriction factor is presented to limit the amount of quantitative error as a function of magnification. KLT, proved to be the most accurate of the proposed methods due to its noise handling capabilities at large magnification factors. TRAC values for each method was computed, where KLT outperformed the image denoising prior to computing the centroid. Scaling factors were computed to compensate for distortion error found in frames as a result of magnification. A linear least squares regression was used to approximate the degrees of accuracy for each of the outlined approaches. Future studies will further investigate automation of image processing parameters with respect to magnification in addition to uncertainty quantification of the methods presented.

Declaration of Competing Interest

The authors declare that they have no known competing financial interests or personal relationships that could have appeared to influence the work reported in this paper.

Acknowledgements

This material is based upon work supported by the National Science Foundation under Grant No. 1762809. Any opinions, findings, and conclusions or recommendations expressed in this material are those of the authors and do not necessarily reflect the views of the National Science Foundation.

References

[1] C. Liu, A. Torralba, W. T. Freeman, F. Durand and E. Adelson, "Motion Magnification," *ACM Trans. Graph.,* vol. 24, pp. 519-526, 7 2005.
[2] N. Wadhwa, M. Rubinstein, F. Durand, W.T. Freeman, Phase-Based Video Motion Processing, ACM Trans. Graphics (TOG) 32 (4) (2013) 1–10.
[3] H.-Y. Wu, M. Rubinstein, E. Shih, J. Guttag, F. Durand, W. Freeman, Eulerian Video Magnification for Revealing Subtle Changes in the World, ACM Trans. Graph. 31 (4) (2012) 1–8.
[4] N. Wadhwa, M. Rubinstein, F. Durand, W.T. Freeman, Riesz Pyramids for Fast Phase-Based Video Magnification, Computational Photography (ICCP), 2014 IEEE International Conference on (2014).
[5] A. Al-Naji, S.-H. Lee, J. Chahl, 2). An efficient motion magnification system for real-time applications, Mach. Vis. Appl. 29 (4) (2018) 585–600, https://doi.org/10.1007/s00138-018-0916-0.
[6] Sushma, M., Gupta, A., & Sivaswamy, J. (2013). Semi-automated Magnification of Small Motions in Videos. In P. Maji, A. Ghosh, M. N. Murty, K. Ghosh, & S. K. Pal (Ed.), *Pattern Recognition and Machine Intelligence* (pp. 417–422). Berlin: Springer Berlin Heidelberg. doi:https://doi.org/10.1007/978-3-642-45062-4_57.
[7] Verma, M., Ghosh, R., & Raman, S. (2018). Saliency Driven Video Motion Magnification. In R. Rameshan, C. Arora, & S. Dutta Roy (Ed.), *Computer Vision, Pattern Recognition, Image Processing, and Graphics* (pp. 89–100). Singapore: Springer Singapore. doi:https://doi.org/10.1007/978-981-13-0020-2_9.
[8] N. Branch, E.C. Stewart, Applications of Phase-Based Motion Processing. *2018 AIAA/ASCE/AHS/ASC Structures*, Structural Dynamics, and Materials Conference (2018) (p. 1948), https://doi.org/10.2514/6.2018-1948.
[9] Chen, J., Davis, A., Wadhwa, N., Durand, F., T. Freeman, W., & Büyüköztürk, O. (2016, 12). Video Camera–Based Vibration Measurement for Civil Infrastructure Applications. *Journal of Infrastructure Systems, 23*, B4016013. doi:10.1061/(ASCE)IS.1943-555X.0000348.
[10] Chen, J., Wadhwa, N., Cha, Y.-J., Durand, F., T. Freeman, W., & Buyukozturk, O. (2015, 6). Modal identification of simple structures with high-speed video using motion magnification. *Journal of Sound and Vibration, 345*. doi:10.1016/j.jsv.2015.01.024.
[11] do Cabo, C. T., Valente, N. A., & Mao, Z. (2020). Motion magnification for optical-based structural health monitoring. In P. Fromme, & Z. Su (Ed.), *Health Monitoring of Structural and Biological Systems XIV. 11381*, pp. 221 – 227. SPIE. doi:10.1117/12.2559266.
[12] Fioriti, V., Roselli, I., Tatì, A., Romano, R., & De Canio, G. (2018, 7). Motion Magnification Analysis for Structural Monitoring of Ancient Constructions. *Measurement, 129*. doi:10.1016/j.measurement.2018.07.055.
[13] A.J. Molina-Viedma, L. Felipe-Sesé, E. López-Alba, F.A. Díaz, 8). 3D mode shapes characterisation using phase-based motion magnification in large structures using stereoscopic DIC, Mech. Syst. Sig. Process. 108 (2018) 140–155, https://doi.org/10.1016/j.ymssp.2018.02.006.
[14] Bao, Y., Seshadri, P., & Mahadevan, S. (2017). Motion magnification for mode shape determination. *58th AIAA/ASCE/AHS/ASC Structures, Structural Dynamics, and Materials Conference, 2017*.
[15] Dorn, C. J., Mancini, T. D., Talken, Z. R., Yang, Y., Kenyon, G., Farrar, C., & Mascareñas, D. (2016). Automated Extraction of Mode Shapes Using Motion Magnified Video and Blind Source Separation. In M. Mains (Ed.), *Topics in Modal Analysis & Testing, Volume 10* (pp. 355–360). Cham: Springer International Publishing. doi:https://doi.org/10.1007/978-3-319-30249-2_32.
[16] Eitner, M. A., Miller, B. G., Sirohi, J., & Tinney, C. E. (2019). Operational Modal Analysis of a Thin-Walled Rocket Nozzle Using Phase-Based Image Processing and Complexity Pursuit. In C. Niezrecki, J. Baqersad, & D. Di Maio (Ed.), *Rotating Machinery, Optical Methods & Scanning LDV Methods, Volume 6* (pp. 19–29). Cham: Springer International Publishing. doi:https://doi.org/10.1007/978-3-030-12935-4_3.
[17] H. Hassoun, J. Hallal, D. Duhamel, M. Hammoud, A.H. Diab, Modal Analysis of a Cantilever Beam Using an Inexpensive Smartphone Camera: Motion Magnification Technique, Retrieved from, Int. J. Mech. Mechatr. Eng. 15 (2021) 52–56, https://publications.waset.org/vol/169.
[18] Á.J. Molina-Viedma, E. López-Alba, L. Felipe-Sesé, F.A. Díaz, 4). Operational Deflection Shape Extraction from Broadband Events of an Aircraft Component Using 3D-DIC in Magnified Images, Shock Vib. 2019 (2019) 1–9, https://doi.org/10.1155/2019/4039862.
[19] A. Sarrafi, Z. Mao, C. Niezrecki, P. Poozesh, Vibration-based damage detection in wind turbine blades using Phase-based Motion Estimation and motion magnification, J. Sound Vib. 421 (2018) 300–318, https://doi.org/10.1016/j.jsv.2018.01.050.
[20] Valente, N. A., Mao, Z., Southwick, M., & Niezrecki, C. (2020). Implementation of Total Variation Applied to Motion Magnification for Structural Dynamic Identification. In D. Di Maio, & J. Baqersad (Ed.), *Rotating Machinery, Optical Methods & Scanning LDV Methods, Volume 6* (pp. 139–144). Cham: Springer International Publishing. doi:https://doi.org/10.1007/978-3-030-47721-9_17.
[21] D.P. Rohe, P.L. Reu, Experimental Modal Analysis Using Phase Quantities from Phase-Based Motion Processing and Motion Magnification, Exp. Tech. 45 (3) (2021) 297–312, https://doi.org/10.1007/s40799-020-00392-7.
[22] Sarrafi, A., & Mao, Z. (2019). Mapping Motion-Magnified Videos to Operating Deflection Shape Vectors Using Particle Filters. In C. Niezrecki, J. Baqersad, & D. Di Maio (Ed.), *Rotating Machinery, Optical Methods & Scanning LDV Methods, Volume 6* (pp. 75–83). Cham: Springer International Publishing. doi:https://doi.org/10.1007/978-3-030-12935-4_8.
[23] Z. Shang, Z. Shen, Multi-point vibration measurement and mode magnification of civil structures using video-based motion processing, Autom. Constr. 93 (2018) 231–240, https://doi.org/10.1016/j.autcon.2018.05.025.
[24] Y. Yang, C. Dorn, T. Mancini, Z. Talken, G. Kenyon, C. Farrar, D. Mascareñas, Blind identification of full-field vibration modes from video measurements with phase-based video motion magnification, Mech. Syst. Sig. Process. 85 (2017) 567–590, https://doi.org/10.1016/j.ymssp.2016.08.041.
[25] P. Poozesh, A. Sarrafi, Z. Mao, P. Avitabile, C. Niezrecki, Feasibility of extracting operating shapes using phase-based motion magnification technique and stereo-photogrammetry, J. Sound Vib. 407 (2017) 350–366, https://doi.org/10.1016/j.jsv.2017.06.003.
[26] Lucas, B. D., & Kanade, T. (1981). An Iterative Image Registration Technique with an Application to Stereo Vision. *Proceedings of the 7th International Joint Conference on Artificial Intelligence - Volume 2* (pp. 674–679). San Francisco, CA, USA: Morgan Kaufmann Publishers Inc. doi:doi/10.5555/1623264.1623280.
[27] G. Fu, W. Bo, X. Pang, Z. Wang, L. Chen, Y. Song, Z. Zhang, J. Li, R. Wu, Mapping shape quantitative trait loci using a radius-centroid-contour model, Heredity 110 (6) (2013) 511–519, https://doi.org/10.1038/hdy.2012.97.
[28] Jianbo Shi and Tomasi. (1994, 6). Good features to track. *1994 Proceedings of IEEE Conference on Computer Vision and Pattern Recognition*, (pp. 593-600). doi:10.1109/CVPR.1994.323794.
[29] A. Sabato, N.A. Valente, C. Niezrecki, Development of a Camera Localization System for Three-Dimensional Digital Image Correlation Camera Triangulation, IEEE Sensors Journal 20 (19) (2020) 11518–11526, https://doi.org/10.1109/JSEN.2020.2997774.

[30] J. Javh, J. Slavič, M. Boltežar, The subpixel resolution of optical-flow-based modal analysis, Mech. Syst. Sig. Process. 88 (2017) 89–99, https://doi.org/10.1016/j.ymssp.2016.11.009.
[31] E. Moya-Albor, J. Brieva, H. Ponce, O. Rivas-Scott, C. Gómez-Peña, Heart Rate Estimation using Hermite Transform Video Magnification and Deep Learning, 2018 40th Annual International Conference of the IEEE Engineering in Medicine and Biology Society (EMBC) (2018) 2595–2598, https://doi.org/10.1109/EMBC.2018.8512879.
[32] V. Srivastava, J. Baqersad, An optical-based technique to obtain operating deflection shapes of structures with complex geometries, Mech. Syst. Sig. Process. 128 (2019) 69–81, https://doi.org/10.1016/j.ymssp.2019.03.021.
[33] Won, J., Huang, P.-C., & Boppart, S. A. (2020, 5). Phase-based Eulerian motion magnification reveals eardrum mobility from pneumatic otoscopy without sealing the ear canal. *J. Physics: Photonics, 2*, 034004. doi:10.1088/2515-7647/ab8a59.
[34] C. Tomasi, T. Kanade, Detection and Tracking of Point Features, Tech. rep., International J. Computer Vision. (1991).
[35] Yongyong, D., Xinhua, H., yujie, Y., & Zongling, W. (2020, 7). Image stabilization algorithm based on KLT motion tracking. *2020 International Conference on Computer Vision, Image and Deep Learning (CVIDL)*, (pp. 44-47). doi:10.1109/CVIDL51233.2020.00016.
[36] Simoncelli, E. P., & Freeman, W. T. (1995, 10). The steerable pyramid: a flexible architecture for multi-scale derivative computation. *Proceedings., International Conference on Image Processing, 3*, pp. 444-447 vol.3. doi:10.1109/ICIP.1995.537667.
[37] Lim, J. S. (1990). *Two-dimensional signal and image processing.* Englewood Cliffs, N. J.: Prentice Hall. Retrieved from http://www.gbv.de/dms/ilmenau/toc/611458640.PDF.
[38] L.I. Rudin, S. Osher, E. Fatemi, Nonlinear total variation based noise removal algorithms, Physica D 60 (1-4) (1992) 259–268, https://doi.org/10.1016/0167-2789(92)90242-F.
[39] Oh, T.-H., Jaroensri, R., Kim, C., Elgharib, M., Durand, F., Freeman, W. T., & Matusik, W. (2018). Learning-Based Video Motion Magnification. In V. Ferrari, M. Hebert, C. Sminchisescu, & Y. Weiss (Ed.), *Computer Vision – ECCV 2018* (pp. 663–679). Cham: Springer International Publishing. doi:https://doi.org/10.1007/978-3-030-01225-0_39.
[40] Wu, X., Yang, X., Jin, J., & Yang, Z. (2018, 7). Amplitude-Based Filtering for Video Magnification in Presence of Large Motion. *Sensors, 18*, 2312. doi:10.3390/s18072312.
[41] A. Chambolle, V. Caselles, M. Novaga, D. Cremers, T. Pock, An introduction to Total Variation for Image, Analysis. 9 (2010), https://doi.org/10.1515/9783110226157.263.